

Searches for new physics in $t\bar{t}$ pair production at the Large Hadron Collider

Candidate

Antonella Succurro

Supervised by

Dr. Aurelio Juste Rozas

Institució Catalana de Recerca i Estudis Avancat

Institut de Física d'Altes Energies

Professore: Lei ha una qualche ambizione?

Nicola: Ma... Non...

Professore: E Allora vada via... Se ne vada dall'Italia. Lasci l'Italia finché è in tempo.
Cosa vuole fare, il chirurgo?

Nicola: Non lo so, non ho ancora deciso...

Professore: Qualsiasi cosa decida, vada a studiare a Londra, a Parigi... Vada in
America, se ha le possibilità, ma lasci questo Paese. L'Italia è un Paese da
distruggere: un posto bello e inutile, destinato a morire.

Nicola: Cioè, secondo lei tra poco ci sarà un'apocalisse?

Professore: E magari ci fosse, almeno saremmo tutti costretti a ricostruire... Invece
qui rimane tutto immobile, uguale, in mano ai dinosauri. Dia retta, vada via...

da La meglio Gioventù di M.T. Giordana (2003)

⁴ Introduccion

⁵

Contents

8	Introduction	ix
9	1 Going beyond the Standard Model	1
10	1.1 Building the Standard Model	1
11	1.2 New Physics Models predicting vector-like quarks	1
12	2 The ATLAS experiment at the Large Hadron Collider	3
13	2.1 The ATLAS detector	6
14	2.1.1 Coordinate system	7
15	2.1.2 Magnets	9
16	2.1.3 Inner detector	9
17	2.1.4 Calorimeters	11
18	2.1.5 Muon spectrometer	14
19	2.1.6 Trigger system	16
20	3 Monte Carlo simulation	19
21	3.1 Parton shower	19
22	3.2 Hadronization	19
23	3.3 Underlying-event	19
24	3.4 Generators	19
25	4 Object reconstruction	21
26	4.1 Tracks	22
27	4.2 Primary vertices	23
28	4.3 Energy clusters	23
29	4.4 Electrons	24
30	4.4.1 Scale factors and energy corrections for analysis	25
31	4.5 Muons	26
32	4.5.1 Scale factors and energy corrections	26

33	4.5.2	Analysis requirements	26
34	4.6	Jets	26
35	4.6.1	Scale factors and energy corrections	27
36	4.6.2	Analysis requirements	27
37	4.6.3	b -tagging	27
38	4.7	Missing Transverse Energy	27
39	4.7.1	Analysis requirements	27
40	5	Searches for vector-like top partner pairs in the single lepton channel	29
41	5.1	General strategy for $T\bar{T}$ pairs searches	29
42	5.2	Data sample and common event preselection	29
43	5.3	Background and signal modeling	30
44	5.3.1	Monte Carlo simulated samples	31
45	5.3.2	Multi-jet background	34
46	5.4	Systematical uncertainties treatment	34
47	6	Preliminary search for $T\bar{T}$ pairs decaying to $Wb + X$	35
48	6.1	Boosted W reconstruction	35
49	6.2	Control regions	35
50	6.3	Event selection	35
51	6.4	Systematics	35
52	7	Preliminary search for $T\bar{T}$ pairs decaying to $Ht + X$	37
53	7.1	Control regions	37
54	7.2	Event selection	37
55	7.3	Systematics	37
56	8	Results	39
57	8.1	Combination	39
58		Conclusions	41
59		A	43
60		B	45
61		C Search for $T\bar{T} \rightarrow Wb + X$ at $\sqrt{7}$ TeV	47
62		Bibliography	49

63 Introduction

64

66 Going beyond the Standard Model

67

68 The Standard Model (SM) of particle physics is the most successful, beautiful and
69 precise theory describing the interactions between fundamental particles. Its validity has
70 been tested by precision measurements at the Large Electron-Positron Collider (LEP) at
71 CERN and confirmed by the observation of all the particles it predicts, including the Higgs-
72 like boson discovered at the Large Hadron Collider (LHC) in July of 2012 which up to now
73 behaves as expected from the SM.

74 What makes the SM “only” and effective theory is the fact that unstabilities appear at
75 high energy scales of the order of the Planck mass. In this Chapter we will show

76 1.1 Building the Standard Model

77 1.2 New Physics Models predicting vector-like quarks

78 [1, 2]

The ATLAS experiment at the Large Hadron Collider

The analyses presented in this dissertation have been performed analyzing data from proton-proton (p-p) collisions at the center of mass energy $\sqrt{s} = 8$ TeV recorded during the year 2012 at the ATLAS experiment [3]. In the following Chapter we will briefly describe the main features of the detector, located at the CERN laboratories in Geneva, Switzerland.

The experimental facilities are situated at Point 1 along the Large Hadron Collider (LHC) [4] 27 km long ring, shown in Figure 2.1. The accelerator tunnel can reach an underground depth of 175 meters and is spread between Swiss and French territory, while the cave where ATLAS is allocated is about 100 meters underground in the CERN Swiss site of Meyrin.

The LHC program was approved by CERN Council in 1994, followed by the approval of the four main experiments physics programs: ATLAS [3] and CMS [5] in 1996; ALICE [6] in 1997; LHCb [7] in 1998. Works towards the installation of the most powerful particle accelerator of the world started when the Large Electron Positron Collider (LEP) was dismantled in 2000 to give up its place in the tunnel to the LHC, which was then fully operational by 2008.

The LHC is composed of eight arcs 2.7 km long, each of which contains 154 dipole magnets, whose function is to bend the beams along the circular trajectory, and 49 quadrupole magnets, that focus the beam. These superconducting magnets operate at a temperature of 1.9 K, maintained by means of liquid Helium vessels. Eight insertions are placed between the arches. Each insertion has a specific role that characterizes its design and can be injection, beam dumping, beam cleaning, or “physics”, i.e. make the beams collide within an experiment.

First proton beams were circulated on 10th September 2008 and right on the verge of getting the first collisions at a center of mass energy $\sqrt{s} = 900$ GeV nine days later, an electrical connection joining superconducting wires of a dipole and a quadrupole failed. This caused the release of liquid Helium in the insulating vacuum, resulting in an explosion that severely damaged the machine. After more than one year devoted to repair the damage

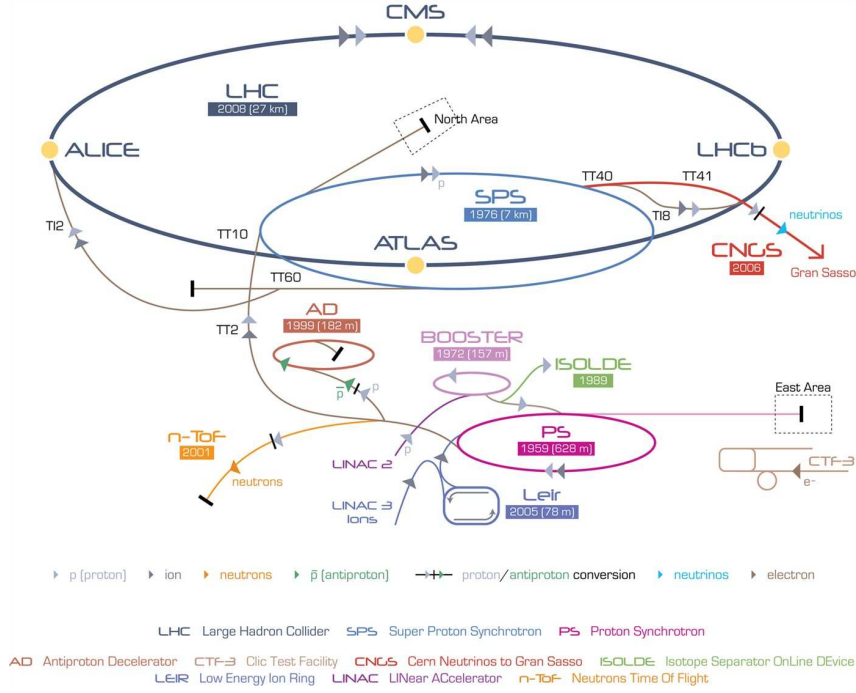


Figure 2.1: A schematic showing the accelerator complex at CERN. Protons are extracted from Hydrogen gas and injected in the first machine, the linear accelerator LINAC2 that starts the acceleration chain. When protons reach an energy of 50 MeV they are injected into the Proton Synchrotron Booster (PSB) and accelerated up to the energy of 1.4 GeV. The second circular accelerator, the Proton Synchrotron (PS) brings the energy of the protons to 25 GeV previous to injecting them into the last machine before the LHC, the Super Proton Synchrotron (SPS). Protons of 450 GeV finally enter the LHC where they are boosted to energies of up to 4 TeV. The four main LHC experiments are shown on the collider ring.

and consolidate the security, on 30th November 2009 the LHC became the world's highest energy particle accelerator¹:

Geneva, 30 November 2009. CERN's Large Hadron Collider has today become the worlds highest energy particle accelerator, having accelerated its twin beams of protons to an energy of 1.18 TeV in the early hours of the morning. This exceeds the previous world record of 0.98 TeV, which had been held by the US Fermi National Accelerator Laboratorys Tevatron collider since 2001. It marks another important milestone on the road to first physics at the LHC in 2010.

The main performance figure of merit for an accelerator is the luminosity, the instantaneous luminosity \mathcal{L} being defined as

$$\mathcal{L} \times \sigma = \frac{dN}{dt} = f \times n \frac{N_1 \times N_2}{A} \times \sigma. \quad (2.1)$$

Here dN/dt is the event rate of a certain process and σ is its cross section. This rate is directly proportional to the the frequency f , the number of bunches n and the number of particles in the two bunches N_1, N_2 , and inversely proportional to the beam cross-section A .

¹<http://press.web.cern.ch/press/PressReleases/Releases2009/PR18.09E.html>

Parameter	designed	2010	2011	2012
Beam energy (TeV/c)	7	3.5	3.5	4
Beta function β^* (m)	0.55	2.0/3.5	1.5/1.0	0.6
Max. No. bunches/beam	2808	368	1380	1380
Max. No. protons/bunch	1.15×10^{11}	1.2×10^{11}	1.45×10^{11}	1.7×10^{11}
Bunch spacing (ns)	25	150	75/50	50
Peak luminosity ($\text{cm}^{-2}\text{s}^{-1}$)	1×10^{34}	2.1×10^{32}	3.7×10^{33}	7.7×10^{33}
Emittance ε_n (μrad)	3.75	2.0	2.4	2.5

Table 2.1: Overview of some parameters for the LHC performance comparing the design values with their time evolution during the first long run operation in 2010-2013 [8].

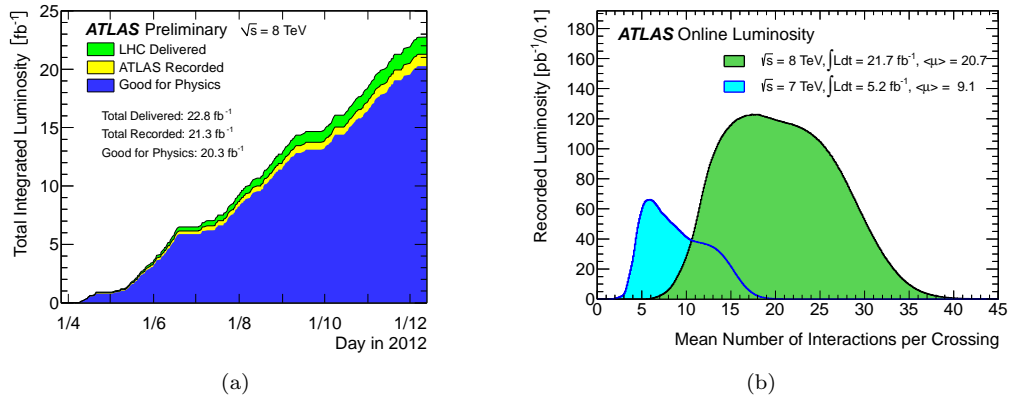


Figure 2.2: (a) Total integrated luminosity versus time delivered by the LHC to ATLAS (in green), recorded by the experiment (in yellow) and selected as “good data” for analysis (in blue) for p-p collisions at $\sqrt{s}=8 \text{ TeV}$. (b) Mean number of interactions per beam crossing during 2011 and 2012 LHC runs, where $\mu = \mathcal{L} \times \sigma_{\text{inelastic}}/f$ depends on the instantaneous luminosity \mathcal{L} , the p-p inelastic cross section $\sigma_{\text{inelastic}}$ and the revolution frequency f . [9]

Integrating over the accelerator active time (a “fill”, when stable beams are kept colliding) gives the *integrated luminosity*, relating the total number of produced events N_{tot} to the cross-section:

$$\int \mathcal{L} dt = \frac{N_{\text{tot}}}{\sigma}. \quad (2.2)$$

In 2012 LHC reached a peak luminosity of $7.7 \times 10^{33} \text{ cm}^{-2}\text{s}^{-1}$ which is more than half the design luminosity, as shown in Table 2.1 together with other parameters relevant for the accelerator performance. Over the last year of data taking before the long shutdown² ATLAS collected about 20 fb^{-1} of p-p collision data at $\sqrt{s}=8 \text{ TeV}$. Figure 2.2(a) shows the delivered luminosity from the start of stable beams until beam dump and the luminosity recorded by ATLAS during stable beam conditions, the difference with respect to the delivered luminosity being due to Data Acquisition (DAQ) inefficiencies. Of the recorded luminosity, only a part

²LHC terminated the p-p program at the end of 2012, operated proton-heavy ion collisions for two months at the beginning of 2013 and then stopped for what is called the first long shutdown. During this two-years time the accelerator and the experiments as well will undergo substantial maintenance and upgrade works, in order to be re-operated in 2015 with higher performance at a higher center of mass energy for particle collisions.

is usable for analysis, and is what is called “good data”, i.e. the data that satisfy Data Quality (DQ) requirements assessed after reprocessing.

In order to increase the luminosity LHC operates with a high number of protons per bunch as well as a high number of bunches per beam and reduces the inter-bunch latency time. This overall defines a set of challenges that physics analysis will face associated to the high luminosity. Even at the detector design stage, the high frequency of collision environment foreseen influenced the choice of radiation resistance material for the experiment sub-systems. Concerning directly the physics instead we can list the main problematics as being *underlying events* and *pile-up*

Underlying events are the product of the hadronic character of p-p hard interaction, where the main collision process is accompanied by secondary parton interactions at low transferred momentum (soft QCD) and are flavor- and color-connected to the hard scattering. They are observed as jets of particles close to the direction of the beam and are in general not separable from the event of interest. Their contribution can be studied with Monte Carlo techniques tuned with data from *minimum bias* events, as perturbative theory does not properly model low momentum QCD.

Pile-up events are distinguished between *in-time* and *out-of-time* pile-up. The first ones come from the multiple inelastic scatterings of protons in the same bunch, as if we consider a cross-section of 80 mb at the nominal luminosity of $10^{34} \text{ cm}^{-2}\text{s}^{-1}$ the number of events per second will be something like a billion. This translates, at a collision frequency of one crossing every 25 ns, to about 20 interactions per crossing that will be detected simultaneously. On the other hand, the inter-bunch time interval is so short that the electronics reading the detector might not keep up with the frequency of collisions, leading to the cumulation of events that happened in different beam crossings.

ATLAS makes use of a three-level trigger system (described in Section 2.1.6) to identify and record only the events of interest, while the pile-up issues are dealt with at the analysis reconstruction level.

2.1 The ATLAS detector

ATLAS (A Toroidal LHC ApparatuS) [3] is a general purpose experiment aimed at exploring a vast range of physics scenarios. It is characterized by a full coverage of the space around the p-p interaction point and complete containment of the particles produced in the collision. Different subsystems are layered concentrically one after the other, each of them pursuing a specific task. Right around the interaction point (IP) where the LHC makes protons collide there is the Vertex Detector, reconstructing charged particles trajectories that are bended by the first solenoid magnet surrounding the Vertex Detector. Particles going through it then encounter the two calorimeter systems, the Electromagnetic and the Hadronic one. Muons are the only particles that will pass the calorimeters material (beyond neutrinos) and a dedicated Muon Spectrometer is the last piece of detector, embedded in a huge toroidal magnet. The detector complex is presented as a schematic in Figure 2.3.

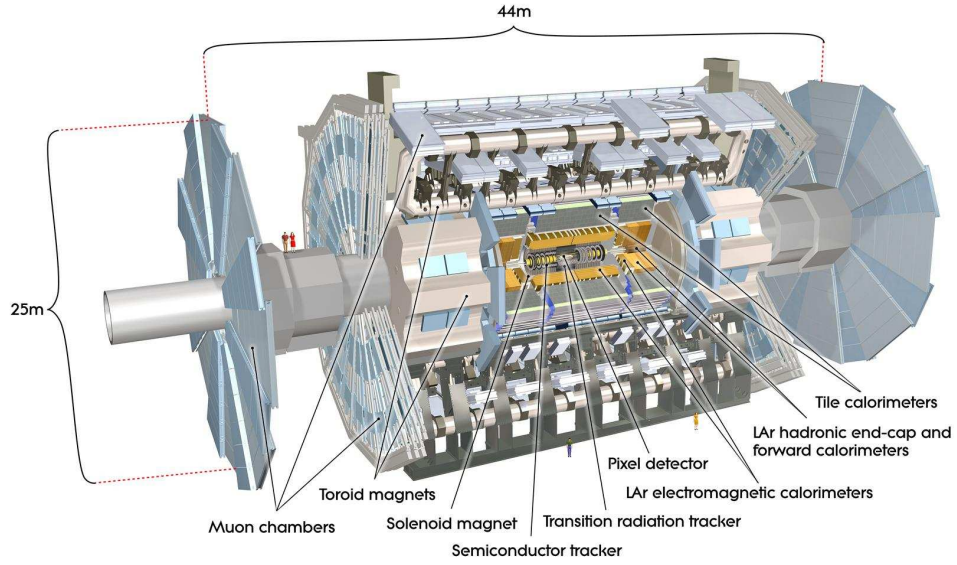


Figure 2.3: Schematic drawing of the ATLAS experiment. The detector subsystem are indicated as well as the total dimensions.

2.1.1 Coordinate system

Protons from the two circulating beams are made to collide in the center of the ATLAS detector, in the region that takes the name of Interaction Point (IP). The IP is taken as the origin of a three dimensional XYZ right-handed coordinate system. The Z axis is tangent to the trajectory of the beams while the XY plane is perpendicular to it and defines a symmetry plane for the detector, dividing it into the A and C sectors, respectively in the positive and negative Z semi-axes. Figure 2.4(a) shows a schematic of the coordinate system.

In terms of polar coordinates, the Z axis is again along the beam axis and in the transverse plane the R and ϕ coordinates are defined with ϕ ranging between $-\pi$ and $+\pi$ with respect to the X axis. In terms of spherical coordinates (see Figure 2.4(b)), the radial vector R originates from the IP, the azimuth ϕ is the same as the polar angle ϕ , and the polar angle θ is measured with respect to the Z axis and ranges between 0 and π .

Since the interaction initial energy is unknown, being dependent on the parton distribution functions for the proton energy, it is useful to define the transverse component of variables of interest³ like the energy and the momentum, being taken as the projection on the XY plane:

$$E_T = E \sin \theta, \quad p_T = p \sin \theta. \quad (2.3)$$

Another common variable used at hadron colliders to describe the polar distribution and

³These quantities transverse initial value will be, indeed, zero, as the protons are accelerated along the Z axis.

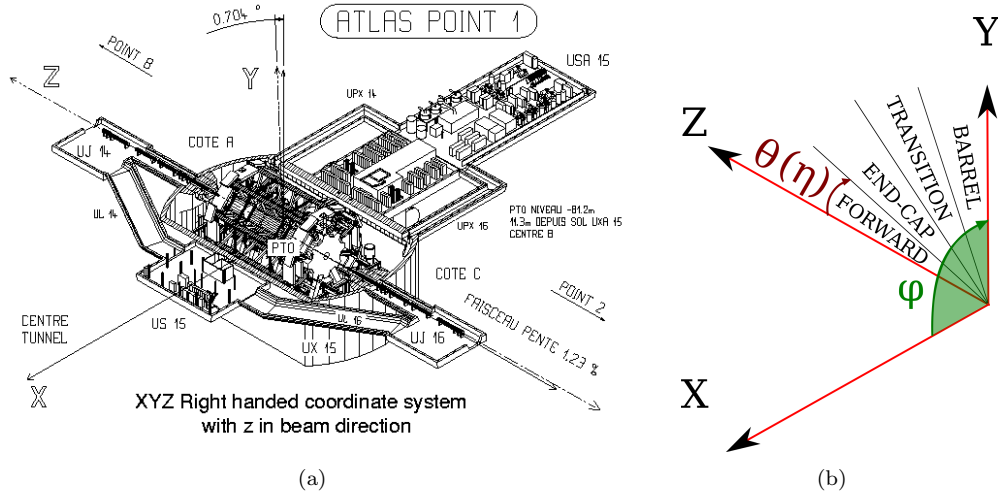


Figure 2.4: (a) Drawing of the ATLAS experiment with the cartesian coordinate system. The positive X axis points towards the center of the LHC ring. The positive Z axis points towards the anti-clockwise circulating direction of beam 2. (b) Simple schematic showing the spherical coordinates and the region definition in terms of the absolute value of the pseudorapidity η . These regions are symmetrical with respect to the transverse XY plane.

preferred to the simple polar angle θ is the pseudorapidity η :

$$\eta \equiv -\ln \left(\tan \frac{\theta}{2} \right); \quad (2.4)$$

which, for relativistic regimes, is equal to the rapidity y :

$$y \equiv \frac{1}{2} \ln \left(\frac{E + p_Z}{E - p_Z} \right); \quad (2.5)$$

and Δy and $\Delta \eta$ are Lorentz invariant. The pseudorapidity is preferred to the rapidity as it does not require knowing the particle mass but only its polar position. The distance between two particles is often referred to in terms of ΔR :

$$\Delta R = \sqrt{\Delta^2 \eta + \Delta^2 \phi}. \quad (2.6)$$

Figure 2.4(b) shows how different pseudorapidity regions are named. Particles along the Z axis have a pseudorapidity $|\eta| = \infty$, particles along the Y axis have a pseudorapidity $|\eta| = 0$. ATLAS has an excellent hermeticity and is able to cover pseudorapidity regions up to $|\eta| = 4.9$. Typically, physics analysis consider objects in the pseudorapidity region $|\eta| < 2.5$. For a quick visualization of the correspondence in terms of polar angle distribution, some pseudorapidity values are reported in Table 2.2.

θ	0°	5°	10°	20°	30°	45°	60°	80°	90°
η	∞	3.13	2.44	1.74	1.31	0.88	0.55	0.175	0

Table 2.2: Pseudorapidity vs polar angle values.

2.1.2 Magnets

ATLAS is provided with four superconducting magnets that allow the measurement of charged particles momenta by curving their trajectory.

A central solenoid sits around the inner detector and produces a 2 T magnetic field along the direction parallel to the beam axis. It is only 45 mm thick (equivalent to 0.66 radiation lengths X_0) and is cooled with liquid Helium, sharing the cryostat with the electromagnetic calorimeter.

Paired to the muon spectrometer, the superconducting air-core toroid magnet (Figure 2.5) has an open structure with eight superconducting toroidal coils in the barrel part and two end-cap systems made of eight coils. The field strength varies strongly with ϕ : in the barrel region ($|\eta| < 1.4$) is 1.5-5.5 Tesla·m; in the end-caps ($1.6 < |\eta| < 2.7$) 1-7.5 Tesla·m. Such configuration of the magnets gives a field orthogonal to the muons trajectory.

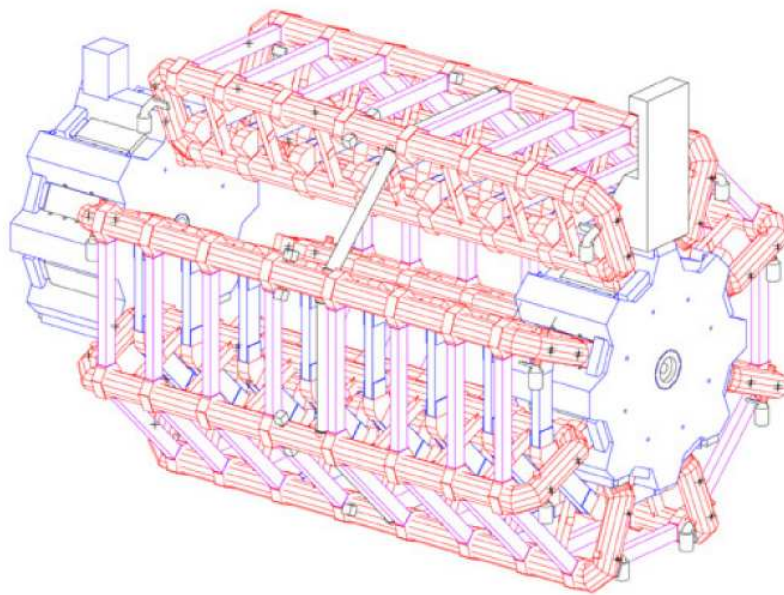


Figure 2.5: Toroidal magnet system.

2.1.3 Inner detector

The Inner Detector (ID) is the subsystem closest to the IP and tracking charged particles arising from collisions allows for the measurement of their momentum and vertex reconstruction with excellent resolution. At the design choices level, radiation resistance had to be taken into account, as well as reducing the amount of material to be placed in front of the calorimeters to avoid spoiling the energy measurement. This quantity varies between 0.5 and 2.5 X_0 depending on the pseudorapidity region, most of it coming from supporting equipment. This material is responsible for photon conversions and electron bremsstrahlung.

The ID is surrounded by the central solenoid magnet (Section 2.1.2) and is composed by three subsystems, from the closest to the furthest from the IP: a pixel detector, a silicon

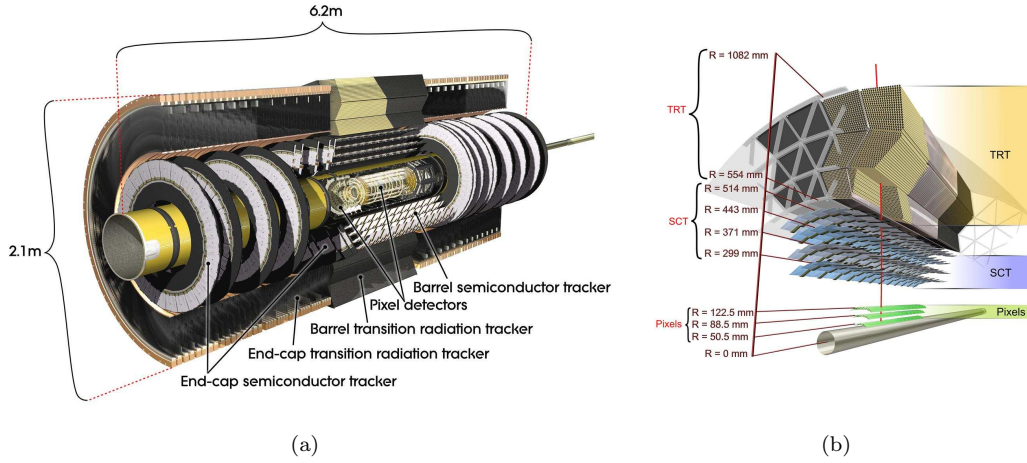


Figure 2.6: (a) Schematic of the ID system. (b) Detailed schematic of the barrel section of the ID showing the three subsystems and reporting the distance to the center of the beam pipe.

strip detector and a straw detector (Figures 2.6(a) and 2.6(b)).

Silicon Detectors

The first subsystem covers the region $|\eta| < 2.5$ and is composed by three cylindrical layers in the barrel region, each of them distant from the beam by 50.5 mm, 88.5 mm and 122.5 mm respectively, and by three concentric discs in the end-cap region, each of them distant from the beam by 49.5 mm, 58.0 mm and 65.0 mm respectively. Each silicon pixel has a size of $50 \times 400 \mu\text{m}^2$ and is $250 \mu\text{m}$ thick, with in total ~ 80.4 million readout channels to achieve a very fine granularity. The precision is of $10 \mu\text{m}$ in $R\phi$ and $115 \mu\text{m}$ in Z and R in the barrel and end-cap region respectively.

The very first layer is called B -layer as, thanks to its position really close to the IP, allows for the reconstruction of secondary vertices associated with the production of short lived particles such as B -hadrons. This information is very useful to identify particle jets from b quarks⁴.

After the three layers of pixel detectors, come four layers of silicon strip detectors. The SemiConductor Tracker (SCT) also covers the region $|\eta| < 2.5$ with a barrel and end-cap design similar to the pixel detector one, being composed by eight silicon bands (two per layer) 128 mm long and $80 \mu\text{m}$ large. It makes use of ~ 6.3 millions readout channels and the resolution achieved is of $17 \mu\text{m}$ in $R\phi$ and $580 \mu\text{m}$ in Z and R in the barrel and end-cap region respectively.

By allowing for four redundant position measurements⁵, the SCT contributes mainly to the momentum reconstruction.

⁴The b -tagging technique will be discussed in

⁵One of the coupled layers is rotated of 40mrad with respect to the other, which is parallel to the axis, giving a small stereo angle for a redundancy in the ϕ coordinate measurement.

Transition Radiation Tracker

In order to reduce the amount of material in front of the calorimeters, and to reduce the construction costs as well, in the third subsystem the semiconductor technology has been substituted with straw detectors. The Transition Radiation Tracker (TRT) consists of thin proportional chambers made of straw polyimide drift tubes, 4 mm in diameter. The drift tubes are filled with a gas mixture composed of: 70% Xenon, 27% Carbon Dioxide, 3% Oxygen. The anode collecting the electrons from the ionized gas at the passage of the charged particle is made of tungsten covered in gold.

In the barrel region the tubes are 144 cm long and placed parallel to the beam axis, while in the end-cap region they are 37 cm long and positioned radially in wheels, with layers of radiator foils alternated to layers of straws. The resolution achieved is of $130 \mu\text{m}$ in $R\phi$ and $Z\phi$ in the two regions respectively. The covered pseudorapidity region is of $|\eta| < 2.0$ and the readout is composed by ~ 351000 channels.

About 36 measurements per track are taken, and since each channel provides two independent thresholds per hit, it is possible to discriminate between electrons and pions, since the firsts will more probably reach the high threshold.

In the end, the combination of the three ID subsystems gives very precise $R\phi$ and Z measurements, as well as good track pattern recognition. The resolution on the transverse momentum, measured with cosmic muon calibration runs [10], is:

$$\frac{\sigma_{p_T}}{p_T} = P_1 \oplus P_2 \times p_T, \quad (2.7)$$

where $P_1 = 1.6 \pm 0.1\%$ and $P_2 = (53 \pm 2) \times 10^{-5} \text{ GeV}^{-1}$. This means a resolution of $\sim 1.6\%$ for tracks with $p_T \sim 1 \text{ GeV}$ and $\sim 50\%$ for tracks with $p_T \sim 1 \text{ TeV}$.

2.1.4 Calorimeters

Particles leaving the ID and surviving the crossing of the central solenoid magnet will face the calorimeter system, depicted in Figure 2.7. The full system is characterized by a coverage in pseudorapidity up to $|\eta| < 5$ and an almost full coverage in ϕ . With its $22 X_0$ and $24 X_0$ of material in the barrel and end-cap regions respectively it is also able to stop most of the non-muon particles from the interaction. Besides particles energy measurement, the calorimeters provide particle identification information, discriminating electrons, photons and jets, and the determination of the missing transverse energy.

Different technologies are used in the barrel, end-cap and forward regions for both the electromagnetic and the hadronic calorimeters. All of them are sampling calorimeters, with a dense medium acting as absorber to stop particles and start showers, and an active material to detect the signal from ionization. For the electromagnetic calorimeters and the forward hadronic calorimeter liquid argon is used as active medium, while the barrel and extended-barrel hadronic calorimeter uses scintillating tiles. The liquid argon is cooled at a temperature of about 88 K, with the use of two sets of cryostats: the barrel electromagnetic calorimeter shares the cryostat with the central solenoid; the end-cap and forward electromagnetic calorimeter and the hadronic end-cap calorimeter share a cryostat in the forward region.

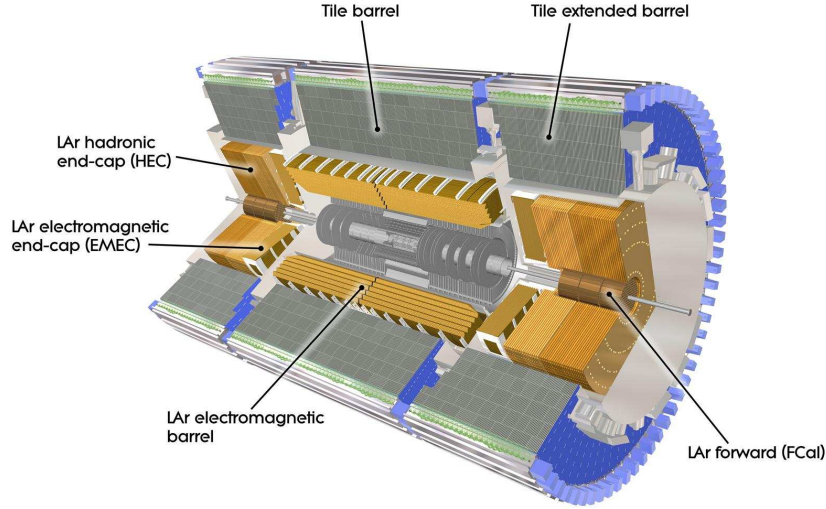


Figure 2.7: Schematic of the calorimeter complex of the ATLAS detector.

271 The processes involved in the shower formation are bremsstrahlung $e^\pm \rightarrow e^\pm + \gamma$ and
 272 pair production $\gamma \rightarrow e^+e^-$. For particles with energies lower than about 100MeV ionization
 273 processes are dominating. In general, these cascade of events continues until a certain
 274 threshold is reached, and the final number of particles produced is proportional to the
 275 energy of the first particle originating the shower.

The performance for the energy resolution is parametrized by the following formula:

$$\frac{\sigma_E}{E} = \frac{a}{\sqrt{E}} \oplus \frac{b}{E} \oplus c, \quad (2.8)$$

276 where the terms of the sum correspond, respectively, to a statistical term related to how
 277 shower develops in the sampling calorimeter; to an instrumental term including readout elec-
 278 tronic rumor effects; to a systematic term that depends on calibration, shower containment,
 279 inactive material and on the linearity of the response as well.

The energy resolution measured in test-beam runs for the liquid argon calorimeters is [11]:

$$\frac{\sigma_E}{E} = \frac{10\%}{\sqrt{E}} \oplus \frac{170 \text{ MeV}}{E} \oplus 0.7\%, \quad (2.9)$$

while for the hadronic barrel calorimeter is [12]:

$$\frac{\sigma_E}{E} = \frac{50\%}{\sqrt{E}} \oplus 3\%. \quad (2.10)$$

280 Electromagnetic calorimeter

281 The electromagnetic calorimeter, also called LAr calorimeter (from Liquid Argon), can
 282 measure electrons and photons energies in the range from 50 MeV and 3TeV. In the barrel

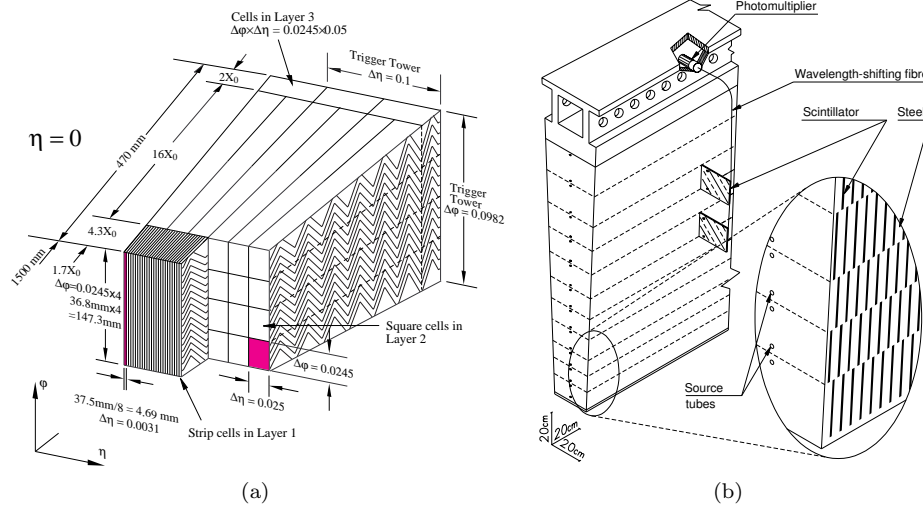


Figure 2.8: (a) Schematic drawing of a module of the Electromagnetic barrel calorimeter. (b) Schematic drawing of a module of the Hadronic barrel calorimeter.

region it is referred to as EMB (ElectroMagnetic Barrel), is divided into two identical semi-barrels EMBA and EMBC separated at $Z=0$ by a 6 mm gap and covers the pseudorapidity region $|\eta| < 1.475$. Two end-cap detectors (EMEC, ElectroMagnetic End-Cap), divided into two coaxial wheels, cover the pseudorapidity regions $1.375 < |\eta| < 3.2$. A pre-sampler, extended over $|\eta| < 1.8$, stands in front of the EMB and allows for the measurement of the energy the particles lost before reaching the EMB i.e. crossing the material of the ID, the central solenoid and the cryostat.

The absorbing material is lead shaped into an accordion geometry to achieve full symmetry in ϕ , as shown in the drawing of Figure 2.8(a). Signal from the ionization produced in the liquid argon is collected by an electrode in the middle of the active material region, fixed into a honeycomb structure.

Three longitudinal regions in the EMB are designed for different tasks. The first sample, $4.3X_0$ long, is finely segmented in η to precisely measure the direction in pseudorapidity of the particles with thin readout strips of $\Delta\eta \times \Delta\phi = 0.0031 \times 0.098$. This helps for photon/ π^0 discrimination and as well for separate close-by γ s from π^0 decay.

The second piece, $16X_0$ long, contains the bulk of electrons and photons energy deposit. It is divided in towers with dimension $\Delta\eta \times \Delta\phi = 0.025 \times 0.0245$ and provides the position measurement of the cluster. The 95% of the energy of the shower is deposited in a matrix of 3×7 towers $\Delta\eta \times \Delta\phi$.

The third layer, $2X_0$ long, is coarsely segmentes and collects the last bit of the longitudinal development of the electromagnetic showers. Towers in this region have a dimension of $\Delta\eta \times \Delta\phi = 0.05 \times 0.0245$.

Also the EMEC is divided in three longitudinal samples (two in the region $1.375 < |\eta| < 1.5$), and besides the lead, also the thickness of the liquid argon layers are varied in the radial direction.

The thickness of the absorber layers depend on the pseudorapidity in order to make par-

tiles entering the system with different incident angles cross the same amount of material.

Hadronic end-cap calorimeter

The Hadronic End-Cap calorimeters (HEC) use copper as passive material and liquid argon as active material, chosen for its radiation hardness in a region ($1.5 < |\eta| < 3.2$) exposed to a significant amount of particle flux. Each HEC is composed by two independent wheels with granularity varying with η : in $1.5 < |\eta| < 2.5$ $\Delta\eta \times \Delta\phi$ is 0.1×0.1 in the first two longitudinal layers, 0.2×0.1 in the last one; in $2.5 < |\eta| < 3.2$ $1.5 < |\eta| < 2.5$ $\Delta\eta \times \Delta\phi = 0.2 \times 0.2$ in all the three samples.

The HECs collect the energy from particles that are not completely contained in the EMECs and in particular are used to reconstruct jets and the missing transverse energy.

Forward calorimeter

The Forward Calorimeter (FCal) cover the very forward region of pseudorapidity $3.1 < |\eta| < 4.9$ making the calorimeter system achieve its good hermeticity and minimize the energy losses. It has an electromagnetic part that uses copper as absorber and two hadronic compartments with tungsten as passive material.

Hadronic barrel calorimeter

The hadronic calorimeter in the barrel and extended barrel region, going up to $|\eta| < 1.7$, is made of scintillating tiles as active material with lead as absorber and is commonly referred to with the name of TileCal. The light in the ultraviolet range that is generated in the tiles is collected through wavelength shifting optical fibres. As can be seen in the drawing of Figure 2.8(b), the tiles are slightly rotated, to allow showers cross them from the side.

TileCal sits just after the electromagnetic calorimeter and measures the energy and position of jets and isolated hadrons. It is divided in depth in three layers with varying length (1.4, 4.1, 1.8 hadronic interaction lengths λ in the barrel and 1.5, 2.6, 3.3 λ in the extended barrel) and segmentation ($\Delta\eta \times \Delta\phi = 0.1 \times 0.1$ in the first two layers, $\Delta\eta \times \Delta\phi = 0.2 \times 0.1$ in the third), and in 64 slices in ϕ , each of $\Delta\phi \sim 0.1$.

The readout channels are grouped into cells that form a pseudo-projective geometry in η .

2.1.5 Muon spectrometer

The most external detector system is the muon spectrometer, a combination of toroidal superconducting magnets (Section 2.1.2) and precision chambers providing a measurement of the momentum of muons in $|\eta| < 2.7$ in addition to the measurement from the ID. It is also equipped with an independent trigger system used for the first event triggering stage (see Section 2.1.6) active in the pseudorapidity region $|\eta| < 2.4$.

Four sub-detectors compose the muon system: Monitored Drift-Tube (MDT) chambers, Cathode Strips Chambers (CSC), Resistive Plate Chambers (RPC) and Thin Gap Chambers (TGC). The layout changes in the barrel and end-cap regions, and is schematically shown in Figure 2.9(b): in the barrel region, chambers are arranged in three cylindrical layers around

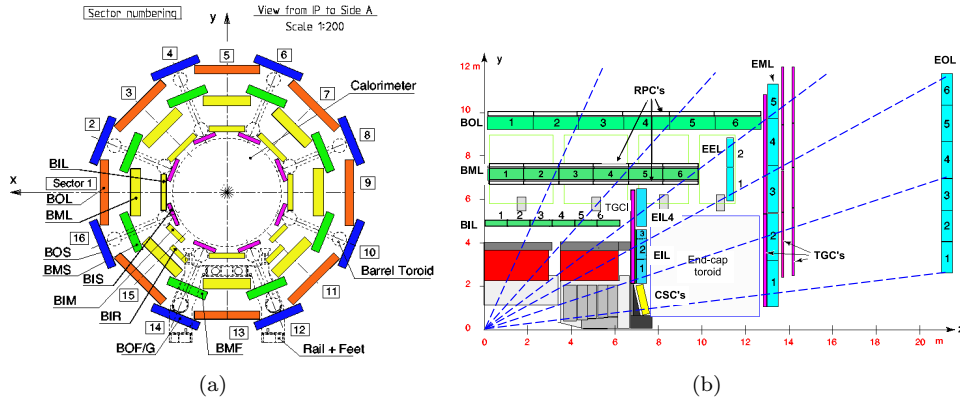


Figure 2.9: (a) Cross section of the barrel muon system. (b) Lateral section of the muon system. Barrel MDTs are shown in green, end-caps MDTs in light blue, CSC in yellow, TGCs in magenta, RPCs in white.

the beam axis, one layer being inside the magnet; in the end-caps these three layers are placed perpendicular to the beam axis.

Detection chambers

MDTs and CSCs are used to detect muons in the pseudorapidity regions $|\eta| < 2.0$ and $2.0 < |\eta| < 2.7$ respectively. MDTs are proportional chambers constituted by aluminium pressurised drift tubes with a diameter of 30 mm and length varying from 0.9 m to 6.2 m. The gas mixture in them is 93% argon and 7% carbon dioxide, the anode is a 50 μm tungsten-rhenium wire producing a radial electric field. Each chamber is composed by a group of six or eight tubes placed transverse to the beam axis. This number of tubes allows for a very good track reconstruction and high reduction of the fake tracks from random associations of background hits, providing a resolution on position of 80 μm .

The CSCs are used at higher η to better deal with the higher particle flux. They are arranged in a system of two disks with eight chambers each. Each chamber contains four multiwire proportional chambers (the CSCs) with wires oriented in the radial direction, spaced by 2.5 mm and in the same gas mixture of argon and carbon dioxide as the MDTs. The cathode strips are oriented one perpendicularly to the anode wires (and gives the precision coordinate) and the other parallelly to the wires (and gives the transverse coordinate). The resolution provided by the interpolation between the charges induced on neighbouring cathode strips ranges between 50 and 70 μm .

Trigger chamber

For trigger purposes detectors quicker than drift tubes are needed⁶. MDTs and CSCs are then coupled with special layers of trigger chambers: in the barrel region, the MDT's second layer is covered on both sides by RPCs, while MDT's third layer is covered by a

⁶Drift-time in tubes with a diameter of $\mathcal{O} \sim 10$ mm can be of ~ 500 ns, too long with respect to the 25 ns spacing of the bunch crossings.

RPC alternatively on the inner and outer side; in the endcaps, TGCs cover the inner side of MDT's first and third layers.

A RPC is a detector with a gas-gap between two resistive bakelite plates separated by 2 mm and containing a gas mixture of $\text{C}_2\text{H}_2\text{F}_4$ (94.7%), $\text{Iso-C}_4\text{H}_{10}$ (5%) and SF_6 (0.3%). RPCs measure six points per coordinate for each particle, quickly collecting the avalanches with two orthogonal sets of pick-up strips that provides a position resolution of 1 cm in each plane and 1 ns time resolution, allowing for individual bunch crossing discrimination. Also RPCs provide the ϕ coordinate for the tracks in the final analysis, since MDTs only give the η coordinate.

TGCs are similar to CSCs, have 1.8 mm wire-to-wire separation and 1.4 mm wire-to-cathode separation. They use a highly quenching gas mixture of CO_2 55% and $\text{n-C}_5\text{H}_{12}$ 45% and provide a spatial resolution of about 1 mm and a time resolution of 5 ns.

2.1.6 Trigger system

It was already introduced at the beginning of this Chapter the issue faced by LHC experiments of dealing with a huge amounts of events at very high frequencies. We remind that considering the nominal LHC luminosity of $10^{34} \text{ cm}^{-2} \text{ s}^{-1}$ a rate of interactions of 1 GHz is expected! This poses serious technical difficulties as the maximum frequency at which data can be recorded is limited to 200 Hz considering the limited capacity for storage.

ATLAS developed a trigger system able to reduce by a factor of 10^6 the amount of data to be kept by selecting only interesting physics events. The system is divided in three levels characterized by increasing sophistication and diminishing speed. At the very first indeed we will need a really quick and simple criterium to reject useless events. The reduced information can then be processed with somehow slower logic by the other two High Level Triggers (HLT). A drawing of the system is shown in Figure 2.10.

Most of the trigger chains used for physics are un-scaled in the sense that all the events passing the selection are kept, but there are also pre-scaled trigger chains that contain either too many events or events considered not physically interesting. These trigger chains are used for checks or calibration rather than physics analysis.

Level 1 trigger

The Level 1 trigger (L1) is completely based on the hardware of the detector, taking information from calorimeters and from the muon spectrometer trigger systems RPC and TGC (Section 2.1.5) at 40 MHz (the frequency of the beam crossing) and reducing it to 75 kHz by choosing events with high transverse momentum or high missing transverse energy.

Using dedicated fast front-end electronics (the typical decision time being less than $2 \mu\text{s}$), calorimeter cells are analogically summed to build calorimetric towers which, if having an energy higher than a certain threshold, will activate a trigger chain.

These trigger chains will then be combined with the information from the muon spectrometer to form the so-called Region of Interest (RoI) that is passed to the next trigger level.

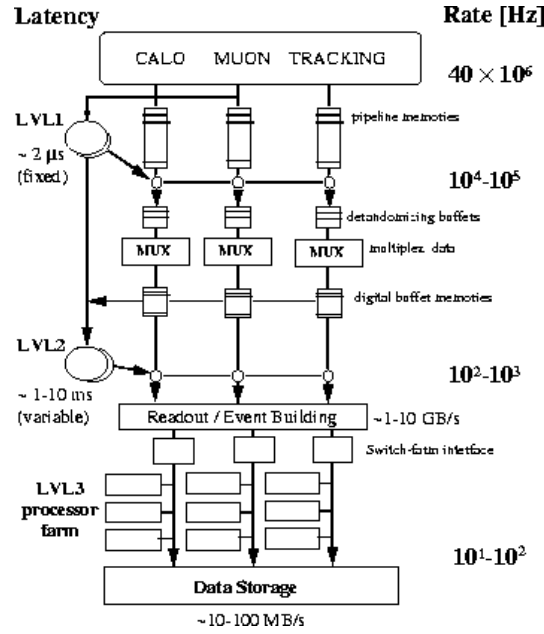


Figure 2.10: Schematic drawing of the three-level trigger system of ATLAS.

408 Level 2 trigger

409 Starting from the RoI, the Level 2 trigger (L2) will reduce the 75 kHz to 3.5 kHz of events
 410 with an average decision time of 40 ns. At this stage the information from the trackers is
 411 incorporated to the RoI to build candidate object (electrons, photons, muons) and better
 412 obtain its position and energy with simplified algorithms quick enough to respect the limit
 413 on the decision time.

414 Level 3 trigger

415 The last trigger, Level 3, is called Event Filter (EF) since at this point the physics objects
 416 are built using the same algorithms as the off-line reconstruction. With an execution time
 417 amounting to 4 s, the EF reduces the event rate to the goal value of 200 Hz.

419 Monte Carlo simulation

420

421 3.1 Parton shower

422 3.2 Hadronization

423 3.3 Underlying-event

424 3.4 Generators

Object reconstruction

427

428 After having described the ATLAS detector in Chapter 2 and the procedure for Monte
 429 Carlo simulation of events in Chapter 3, we understand that what we deal with when we talk
 430 about “data” is raw digital signals from the detector, either the real one or the simulated
 431 one.

432 In the following Chapter we will explain how, starting from these outputs, objects are
 433 reconstructed to be used in physics analyses [13]. This process is what is called “offline event
 434 reconstruction” since it is not done in real time, due to the time required by the algorithms
 435 to perform their tasks.

436 In general we could describe the full procedure as subdivided into three main steps: a
 437 pre-reconstruction stage where the electronic signals are translated into measurements; a
 438 pattern-recognition step where the measurements are assembled into the building blocks of
 439 particles, e.g. tracks and energy clusters; a particle identification final leg where the full
 440 detector information elaborated is combined to match a candidate physics object (electrons,
 441 muons, jets and the missing transverse energy E_T^{miss}).

442 The expected signatures for the various particles in terms of interaction with the detector
 443 system are schematically shown in Figure 4.1.

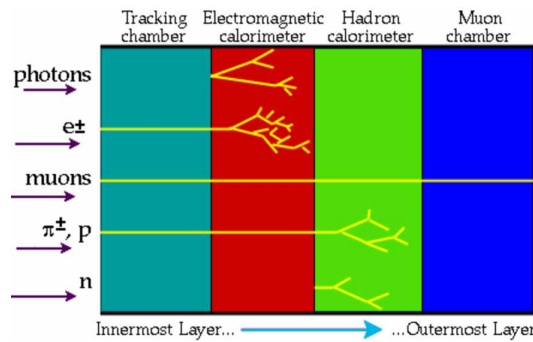


Figure 4.1: Drawing illustrating how particles are detected in the ATLAS sub-systems.

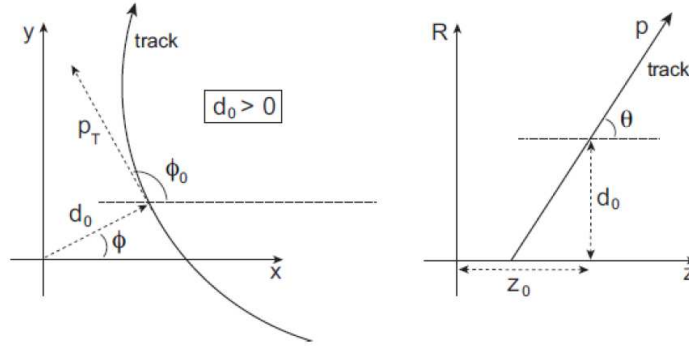


Figure 4.2: Schematic drawings of the parameters used for track reconstruction in the XY and RZ planes (left and right respectively) where the origin is the beam spot, i.e. where the protons collide and interact.

4.1 Tracks

Particle trajectories (“tracks”) are used both to reconstruct the particle itself, giving the momentum measurement, and to identify the interaction vertices. The parameters describing a track are: q/p , the charge divided by the momentum; θ , or more used η , the angle with respect to the Z axis in the RZ plane measured from the perigee¹; ϕ_0 , the angle with respect to the X axis in the XY plane measured from the perigee; d_0 , the impact parameter, or perigee with respect to the Z axis in the XY plane; z_0 , Z component of the perigee. These parameters are shown in the double-view drawing of Figure 4.2.

In order to reconstruct the track, the first step is to retrieve the information from the ID hits, which are converted into three-dimensional space points. Then, the *inside-out* algorithm [14] is used, starting from a seed of three aligned hits in the pixel detector or in the SCT. From there, a path is formed along the seed directional information adding space points one by one. This is done by using a Kalman filter algorithm [15] which checks progressively the compatibility between the track (also progressively updated) and the new point. The five track parameters described before are also computed at this step. A cleaning procedure then rejects incomplete tracks or tracks sharing hits with others, or composed by false space points. The candidate tracks are extended into the TRT and re-fitted taking into account the effects from the interaction of the charged particle with the detector material.

A second algorithm, called *outside-in*, is applied in order to better reconstruct tracks from secondary charged particles. This algorithm does the opposite of the inside-out one, taking as seeds hits in the TRT (the ones not associated to any track candidate in by the inside-out reconstruction) and extrapolating back to the SCT and pixel detector.

¹The perigee is the point of the track closest to the origin.

4.2 Primary vertices

In general, a primary vertex (PV) is identified by the tracks associated to it. The reconstruction is performed via an iterative procedure [16] starting from a seed defined as the maximum in the distribution of the z_0 parameter of reconstructed tracks. After tracks are assigned to the PV with the aid of an iterative χ^2 fit, the ones that fall out of more than 7σ from the PV are used to seed another PV until no track is left without being assigned to a vertex (one track can be associated to more than one vertex).

A PV must have at least two associated tracks and its position must be consistent with the beam collision region in the XY plane. The hard-scatter PV is chosen as the one with the highest sum of squared transverse moments of the tracks. The other reconstructed PVs are identified with pile-up interactions. Another kind of vertices, not compatible with the requirement of coming from close to the proton collision spot, are the secondary vertices, originating from the decay of short-lived particles. These vertices are useful to identify B -hadrons and will be described in Section 4.6.3.

As can be expected, high pile-up environments deteriorate the performance of vertex reconstruction, as more fake tracks are introduced and nearby interaction might lead to the misreconstruction of distinct vertices as a single one [17].

4.3 Energy clusters

With the name “energy cluster” we generically refer to energy deposits in the calorimeter cells that are grouped together on the basis of some criteria [18]. In particular, we are interested in *topological clusters* and *electromagnetic towers*, used respectively for jets and electron/photon reconstruction.

Topological clusters, abbreviated as “topoclusters”, are built from neighboring calorimeter cells starting from a seed deposit with a signal (S , the cell measured energy) to noise (N , the RMS of the cell noise distribution) ratio higher than a certain threshold. Cells with $S/N \geq 4$ are taken as seeds, and starting from the one with the highest S/N all the neighboring cells with $S/N \geq 2$ are added to the topocluster. Topoclusters are treated as massless and their energy at the electromagnetic scale is the sum of the constituent cells. Their position and direction parameters are obtained from a weighted sum of the constituent cells’ pseudorapidity and azimuth angle based on the absolute value cell’s energy. Since energy measurement can be negative (due to noise fluctuations), clusters with negative energies are rejected.

Towers are built using the *sliding window* algorithm [19] starting from single energy deposits in the EM calorimeter middle layer of size $\Delta\eta \times \Delta\phi = 0.025 \times 0.025$. As schematically shown in Figure 4.3, a window of 3×5 cell units is defined, centered on the maximum of energy and finally expanded to optimize the cluster reconstruction, with a size that depends on the object (electron or photon) and the position in the detector (3×7 in regions with $|\eta| < 1.4$ and 5×5 elsewhere).

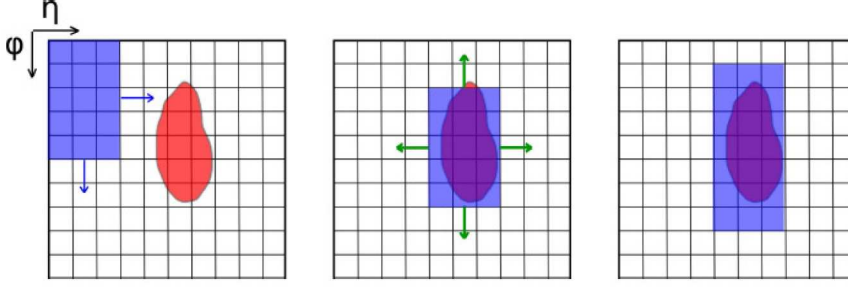


Figure 4.3: The three steps of the sliding window algorithm.

4.4 Electrons

Electrons [19] are reconstructed for pseudorapidities up to $|\eta| = 2.47$, where information from the ID is available, matching a track (see Section 4.1) with a cluster in the electromagnetic calorimeter reconstructed with the sliding window algorithm (see Section 4.3). In order to account for bremsstrahlung losses the matching is done within a region of dimension $\Delta\eta \times \Delta\phi = 0.05 \times 0.10$ and if more candidate tracks are matched, of all the ones with hits in the silicon detectors the track with the smallest ΔR with respect to the energy cluster is chosen. In addition, the track momentum has to be compatible with the cluster energy, which is calibrated to the electromagnetic scale derived from Monte Carlo based corrections (to account for dead material losses), test-beam studies and calibration from $Z \rightarrow ee$ events [20, ?].

In general, electron can be distinguished from hadrons thanks to various characteristics of their shower development: electrons deposit the most of their energy in the second layer of the EM calorimeter; the width of their shower is narrower; they have smaller hadronic leakage²; the E/p variable (ration of cluster energy and track momentum) is higher.

Some difficulties arise when dealing with π^0 and η particles, which decay into two γ s that produce two close showers reconstructed as a single one in the second layer of the EM calorimeter, and in general with jets faking electrons from, e.g. QCD processes. There are then six different electron definitions to help separate real electrons from fake ones, described in the following ordered from the looser requirements to the tightest. Performance studies on electron reconstruction and identification where done using 2010 data and Monte Carlo $Z \rightarrow ee$ and $W \rightarrow e\nu$ events [19].

Loose electrons lie in the pseudorapidity region $|\eta| < 2.47$ and have low hadronic leakage and requirements on the variables defining the shower shape. The identification efficiency is high but the jet rejection is low (about 500).

Loose++ electrons are **loose** electrons whose track has at least one hit in the pixel detector and at least 7 hits in the combined silicon detectors and the $|\eta_{\text{firstEM}}|$ distance between the track extrapolated to the first EM layer and the matched cluster is lower than 0.015. The identification efficiency is similar to the loose one but the rejection is ten times

²The hadronic leakage is the ratio of the transverse energy reconstructed in the first layer of the hadronic calorimeter to the total transverse energy reconstructed in the EM calorimeter.

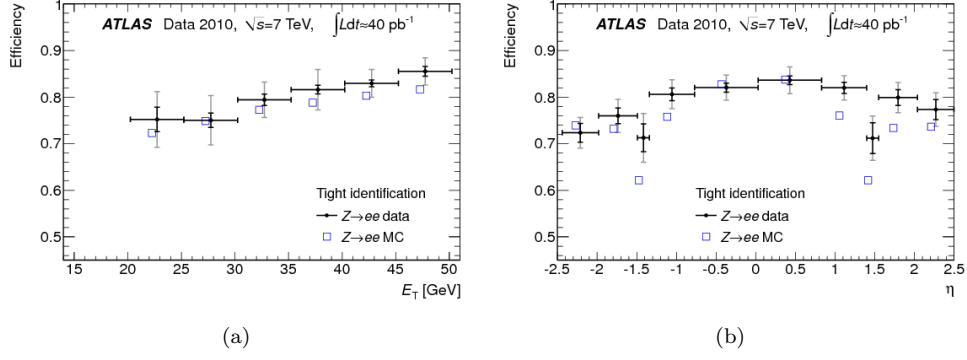


Figure 4.4: Tight electron identification efficiencies measured from $Z \rightarrow ee$ events and predicted by MC as a function (left) of E_T (integrated over $|\eta| < 2.47$ excluding the transition region $1.37 < |\eta| < 1.52$ and (right) of η and integrated over $20 < E_T < 50$ GeV. [19]

higher.

Medium electrons are **loose++** electrons where additional requirements on shower shape are made as well as on their tracks: $|d_0| < 5$ mm and $|\eta_{\text{firstEM}}| < 0.01$. The efficiency drops to 88% and the rejection is higher than the previous.

Medium++ electrons are **medium** electrons whose track has at least one hit in the first pixel detector layer, a requirement that allows to reject electrons from photon conversion. Charged hadrons contamination is reduced by discarding candidates whose track has a low fraction of high-threshold TRT hits. In addition, $|\eta_{\text{firstEM}}| < 0.005$ and stricter cuts are applied to shower shaper of clusters in $|\eta| < 2.01$. The efficiency is about 85% and rejection is about 50×10^3 .

Tight electrons are **medium++** electrons with additional requirements on the distance between the track and the matched cluster ($|\Delta\phi| < 0.02$, $|\Delta\eta| < 0.005$) and on the E/p variable. Stricter cuts are imposed on the fraction of high-threshold TRT hits and on the impact parameter ($|d_0| < 1$ mm). The efficiency drops to 75% and the rejection is higher than the previous one.

Tight++ electrons are **tight** electrons with asymmetric $\Delta\phi$ cuts, which give both better efficiency and rejection.

In addition, to suppress further the QCD multijet background, isolation cuts are imposed both as calorimeter (using the energy in a cone of size $\Delta R < 0.2$, **EtCone20**) and track isolation (using the scalar sum of p_T s from tracks within a cone of $\Delta R < 0.3$, **PtCone30**).

4.4.1 Scale factors and energy corrections for analysis

For our analyses [21], electrons in the transition region $1.37 < |\eta_{\text{cluster}}| < 1.52$ with inactive material are excluded. Electrons are required to satisfy **tight++** criteria and to have $E_T = E_{\text{cluster}} / \cosh \eta_{\text{track}} > 25$ GeV and $z_0 < 2$ mm. The **EtCone20** and **PtCone30** isolation cuts are chosen to give 90% efficiency. In addition, jets (see Section 4.6) within $\Delta R = 0.2$ of the selected electron are discarded, and if an additional jet with $p_T > 25$ GeV and $|JVF| > 0.5$ is found within $\Delta R = 0.4$, then the electron is rejected. The electron is

matched to the single electron trigger `EF_e24vhi_medium1` combined with a logical OR to the `EF_e60_medium1` trigger, which recovers some efficiency loss at $E_T > 80$ GeV.

The efficiency in selecting electrons can be factorized as:

$$\varepsilon = \varepsilon_{\text{reco}} \cdot \varepsilon_{\text{tight++}} \cdot \varepsilon_{\text{isolation}} \cdot \varepsilon_{\text{trigger}} \quad (4.1)$$

where the various components represent respectively: the efficiency in reconstructing the electron in terms of track-cluster match, track quality and hadronic leakage; the efficiency for the `tight++` identification criteria; the efficiency for the isolation cuts; the efficiency from trigger selection. Scale factors are derived in bins of (η, E_T) , and the trigger scale factors are separated into four data-taking periods (A-B3, B4-D3 without C1-C5, C1-C5 and D4+). The efficiency scale factors are applied as weights to Monte Carlo events.

The electron energies in data are corrected using scale factors $\alpha(\eta)$ derived from data-to-simulation comparison in $Z \rightarrow ee$ events in order to match the Z boson mass peak.

Muons

Track segments reconstructed in the muon spectrometer are matched to tracks from the ID to build muon candidates. The combined tracking information has to give $p_T > 25$ GeV and $|\eta| < 2.5$, and z_0 has to be lower than 2 mm. The muon radial distance from any selected jet is required to be $\Delta R > 0.4$.

A p_T -dependent track-based isolation condition is defined as follows: the scalar p_T sum of all tracks (except for the muon track itself) in a cone of variable radius $R = 10 \text{ GeV}/p_T^\mu$ around the lepton must be less than 5% of the muon p_T . This isolation requirement works well also in high pile-up events or in the case the muon is close to a jet.

4.5.1 Scale factors and energy corrections

4.5.2 Analysis requirements

Jets

Jets from quark hadronization are reconstructed using the anti- k_t algorithm [22, 23, 24] with a radius parameter $R = 0.4$ (from which the algorithm is often referred to as anti- k_t4) using calorimeter energy deposits³ corrected for effects of non-compensation, dead detector material and out-of-cluster leakage using local cluster calibrations [25, 26].

To subtract contributions from in-time and out-of-time pile-up interactions a correction is applied parameterized according to the number of primary vertices in the event and the number of average interactions in the luminosity block ($\langle \mu \rangle$) as a function of jet pseudorapidity. Jets are finally calibrated to the hadronic scale using p_T - and η -dependent correction factors derived from Monte Carlo simulation [27]. For the analyses that we will present, only jets with $p_T > 25$ GeV and $|\eta| < 2.5$ are considered.

A variable called “jet vertex fraction” (JVF) is defined as the fraction of the sum of p_T of tracks with $p_T > 1$ GeV associated with the jet that comes from tracks originating from the primary vertex. By requiring $\text{JVF} > 0.5$ we avoid selecting jets from in-time pile-up events.

Since energy deposits from electrons can be reconstructed as jets, if jets are found within ΔR of 0.2 of a selected electron, the jet closest to the lepton is discarded in order to avoid double-counting of electrons as jets. After this one jet has been removed, electrons that lie within $\Delta R < 0.4$ of the jets remaining are removed.

4.6.1 Scale factors and energy corrections

4.6.2 Analysis requirements

4.6.3 b -tagging

A technique to identify jets from the hadronisation of bottom quarks, called b -tagging [28], is used. It makes use of multivariate techniques combining the information from secondary and tertiary decay vertices found within the jet and from the impact parameters of displaced tracks to obtain a b -tagging weight that discriminates between b and not- b jets. A working point for this weight is chosen by finding a compromise between a good efficiency (the ratio between tagged b -jets and true b -jets) and a high light-jet rejection (the inverse of the number of light-jets misidentified as b -jets). For our analyses, a working point corresponding to 70% efficiency, ~ 130 light-jet rejection and a charm-jet rejection of 5 is chosen⁴

4.7 Missing Transverse Energy

To estimate the momentum of invisible particles in the event, the missing transverse energy E_T^{miss} [29] is defined by first matching each calorimeter energy deposit with a high- p_T lepton or jet. After the energies of these objects are corrected accordingly to the respective calibration constants, the calorimeter clusters that did not get associated with any high- p_T object are calibrated for energy losses in dead material regions and for the different response to the electromagnetic and hadronic components of particle showers. Finally the E_T^{miss} is computed from the combination of the vector sum of the calibrated cluster momenta and a term associated with muon momenta.

4.7.1 Analysis requirements

⁴These values refer to jets with $p_T > 20$ GeV and $|\eta| < 2.5$ in simulated $t\bar{t}$ events.

622 Searches for vector-like top partner 623 pairs in the single lepton channel

624

625

626 In the following Chapter we will describe two searches for vector-like top partners $T\bar{T}$
627 pairs performed in the single lepton¹ channel. These analyses are optimized for different
628 final states and are thus complementary. The first search focuses on decay channels with
629 high BR to Wb and is performed using the full dataset of p-p collisions at the center of mass
630 energy of $\sqrt{s}=8$ TeV collected during 2012 at the ATLAS detector, consisting in 20.34 fb^{-1} ,
631 while the preliminary search for vector-like top partners with high BR to Ht uses a partial
632 dataset of the same data, amounting to 14.3 fb^{-1} .

633 The Chapter is organized as follows: first Section 5.2 introduces the common event pre-
634 selection for data and few general concepts in the analyses design; Section 5.3.1 presents the
635 Monte Carlo samples used in the searches, which are in general common to both analyses
636 with only few exceptions that are reported; Section 5.3.2 describes how the multi-jet back-
637 ground from QCD events is obtained. Finally, the two analyses are detailed in Section ?? and
638 Section ??, which illustrate the event selection criteria, the background modeling estimation,
639 the systematics affecting the analysis, the statistical treatment and the results.

640 5.1 General strategy for $T\bar{T}$ pairs searches

641 5.2 Data sample and common event preselection

642 The data from p-p collision events recorded at the ATLAS experiment during 2012
643 at a center of mass energy of $\sqrt{s} = 8$ TeV are considered. Physics object definitions were
644 previously discussed in Section ?. Events collected during stable beam periods are required
645 to pass data quality requirements and single lepton trigger selection. In order to maximize

¹From now on, with the word “lepton” we will mean only either electron or muon, assumed to come from the leptonic decay of a W boson with its associated neutrino, which is considered to be the only particle contributing to the transverse missing energy E_T^{miss} .

	Wb	Ht	Zt
Wb	4 (2)	6 (4)	6 (2/4)
Ht	6 (4)	8 (6)	max: 8 (4/6) min: 6 (2)
Zt	6 (2/4)	max: 8 (4/6) min: 6 (2)	max: 8 (2/6) min: 6 (2/4)

Table 5.1: Jets (b -jets) multiplicities in the various possible final states. Z boson decays 55% hadronically, 15% of the times into $b\bar{b}$, therefore the min/max number of b -jets is reported. Highlighted are the channels that after the orthogonality cut will contribute to the $T\bar{T} \rightarrow Wb+X$ analysis.

trigger efficiency, different transverse momentum threshold triggers are combined through a logical OR, with the lower p_T ones including isolation requirements that result in inefficiencies for high p_T lepton candidates, recovered with the use of the higher threshold triggers. The electron triggers have p_T thresholds of 24 and 60GeV, the muon ones of 24 and 36GeV.

After passing trigger requirements, events with more than one lepton are discarded. In addition, the only lepton of the event has to match within $\Delta R < 0.15$ the triggered one. As basic preselection, four jets satisfying the conditions described in Section 4.6 are required, at least one of them being tagged as a b -jet.

In order to suppress the multi-jet background from QCD processes, combined cuts on the E_T^{miss} and on the transverse mass of the leptonically decaying W boson m_T^2 are defined: $E_T^{\text{miss}} > 20 \text{ GeV}$ and $E_T^{\text{miss}} + m_T > 60 \text{ GeV}$.

At this point, a simple consideration about the typical expected jet (and b -jet) multiplicity is made so as to define an orthogonality cut between the two analyses. Table 5.1 shows the number of jets (b -jets) per decay channel combinations of $T\bar{T}$ pairs, in the case of single lepton selection with at least four jets (i.e. one W boson will always decay into lepton and neutrino, and Z boson decay to neutrinos is excluded in the $WbZt$ channel) and assuming that the Higgs boson decays to a bottom quark-antiquark pair. To avoid overlap between selected events from the two analyses, in the $T\bar{T} \rightarrow Wb + X$ analysis events with ≥ 6 jets and ≥ 3 b -jets are rejected³.

5.3 Background and signal modeling

The main background for both analyses is $t\bar{t}$ production with jets ($t\bar{t}$ +jets in the following) and different choices for the generator are made in the analyses because of the specific needs of having well modeled regions. In the case of the $t\bar{t}$ +jets background prediction for the $T\bar{T} \rightarrow Ht + X$ analysis further corrections to match the data are applied, due to a mis-modeling in the heavy- and light-flavour content of the simulated sample (see Section 7.2).

² $m_T = \sqrt{2p_T^\ell E_T^{\text{miss}}(1 - \cos \Delta\phi)}$, with p_T^ℓ being the transverse momentum (energy) of the muon (electron) and $\Delta\phi$ the azimuthal angle separation between the lepton and the direction of the missing transverse momentum.

³As will be explained later in Section 7.2, another orthogonality cut will be applied in the low b -jet multiplicity channel of the $T\bar{T} \rightarrow Ht + X$ analysis.

671 W boson production in association with jets (W +jets in the following) and multi-jet
 672 events from QCD processed also contributes, the latter sneaking into the event selection via
 673 the misidentification of a jet or a photon as an electron or the presence of a non-prompt
 674 lepton from, e.g., semileptonic b - or c -hadron decay. Other background smaller components
 675 are single top quark, Z +jets, diboson (WW, WZ, ZZ), and $t\bar{t}$ production associated with a
 676 vector or Higgs boson.

677 All event generators using HERWIG [?] are also interfaced to JIMMY v4.31 [?] to simulate
 678 the underlying event. With the exception of the signal samples, all simulated samples utilise
 679 PHOTOS 2.15 [?] to model photon radiation and TAUOLA 1.20 [?] to model τ decays.

680 All simulated samples include multiple p-p interactions and go through the GEANT4 [?]
 681 detector geometry and response simulation [?] with the exception of the signal samples, for
 682 which a fast simulation of the calorimeter response is used.

683 All simulated samples are then processed through the same reconstruction software as
 684 the data and are reweighted to match the instantaneous luminosity profile in data.

685 5.3.1 Monte Carlo simulated samples

686 $t\bar{t}$ MC@NLO

687 Simulated samples of $t\bar{t}$ pair production in association with jets ($t\bar{t}$ +jets or simply $t\bar{t}$
 688 in the following) are generated with MC@NLO v4.01 [?, ?, ?] using the CT10 set of
 689 parton distribution functions (PDFs) [?], with the parton-shower and fragmentation steps
 690 being performed by HERWIG v6.520 [?]. The top quark mass is assumed to be equal to
 691 172.5 GeV and the samples are normalized to approximate next-to-next-to-leading-order
 692 (NNLO) theoretical cross section [?]; the cross section used has been computed with HATHOR
 693 1.2 [?] using the MSTW2008 NNLO PDF set [?] and is $\sigma_{t\bar{t}} = 238^{+22}_{-24}$ pb, where the total
 694 uncertainty results from the sum in quadrature of the scale and PDF+ α_S uncertainties
 695 according to the MSTW prescription [?]. This is the $t\bar{t}$ used in the $T\bar{T} \rightarrow Wb + X$ analysis.

696 $t\bar{t}$ Alpgen

697 Simulated samples of $t\bar{t}$ +jets are generated using the ALPGEN v2.13 [?] leading-order
 698 (LO) generator and the CTEQ6L1 PDF set [?], with parton shower and fragmentation
 699 modelled through HERWIG v6.520 [?].

700 A parton-jet matching scheme called “MLM matching” [?] is used in order to avoid
 701 double-counting of partonic configurations eventually generated both at the matrix-element
 702 calculation level and at the parton-shower evolution step.

703 Separate samples are generated for $t\bar{t}$ +light jets ($t\bar{t}$ +light or $t\bar{t}$ +LF in the following, from
 704 “light flavour”) with up to three additional light partons (u, d, s quarks or gluons), and for
 705 $t\bar{t}$ +heavy-flavour jets ($t\bar{t}$ +HF in the following), including $t\bar{t}b\bar{b}$ and $t\bar{t}c\bar{c}$. An algorithm based
 706 on the angular separation between the extra heavy quarks is used to remove the overlap
 707 between $t\bar{t}q\bar{q}$ ($q = b, c$) generated from the matrix element calculation and from parton-
 708 shower evolution in the $t\bar{t}$ +light samples is employed: matrix-element prediction is chosen
 709 over the parton-shower one when $\Delta R(q, \bar{q}) > 0.4$, else vice-versa.

Again a top quark mass of 172.5 GeV is assumed, and normalisation to the NNLO theoretical cross section is used (see 5.3.1)

W/Z +jets

Simulated samples of W/Z boson production in association with jets (W/Z +jets in the following) are generated with up to five additional partons using the ALPGEN v2.13 [?] LO generator and the CTEQ6L1 PDF set [?], interfaced to HERWIG v6.520 for parton showering and fragmentation.

“MLM matching” is used also here to avoid double-counting of partonic configurations between matrix-element calculation and parton showering.

The W +jets samples are generated separately for W +light jets, $Wb\bar{b}$ +jets, $Wc\bar{c}$ +jets, and Wc +jets, with the relative contributions normalized using the fraction of b -tagged jets in W +1-jet and W +2-jets data control samples [?], while the Z +jets samples are generated separately for Z +light jets, $Zb\bar{b}$ +jets, and $Zc\bar{c}$ +jets and normalized to the inclusive NNLO theoretical cross section [?].

Overlap between $W/Zq\bar{q}$ +jets ($q = b, c$) events generated from the matrix element calculation and those generated from parton-shower evolution in the W/Z +light jets samples is avoided via an algorithm analogous to the one used for $t\bar{t}$ Alpgen.

For the W +jets background, a normalisation from data for the shapes obtained from the simulation is derived since the simulation overestimates the number of W +jets events by up to $\sim 20\%$, depending on the jet multiplicity.

By exploiting the predicted asymmetry between W^+ +jets and W^- +jets production in p-p collisions [?], the total number of W +jets events in data ($N_W = N_{W^+} + N_{W^-}$), can be estimated based on the measured difference between the number of positively- and negatively-charged W bosons, $(N_{W^+} - N_{W^-})_{\text{meas}}$, and the asymmetry predicted from the simulation:

$$N_W = \left(\frac{N_{W^+} + N_{W^-}}{N_{W^+} - N_{W^-}} \right)_{\text{MC}} (N_{W^+} - N_{W^-})_{\text{meas}} \quad (5.1)$$

Events are categorised in terms of multiplicity of b and c jets and scale factors are derived using Equation 5.1. The fraction of W +light jets events is scaled accordingly in order to preserve the overall normalisation of the W +jets background before b tagging.

Other backgrounds

Simulated samples of single top quark backgrounds corresponding to the s -channel and Wt production mechanisms are generated with MC@NLO v4.01 [?, ?, ?] using the CT10 PDF set [?]. In the case of t -channel single top quark production, the ACERMC v3.8 LO generator [?] with the MRST LO** PDF set is used.

Simulated samples of $t\bar{t}$ produced in association with a W or Z boson ($t\bar{t}V$ ($V = W, Z$) in the following) are generated with the MADGRAPH v5 LO generator [?] and the CTEQ6L1 PDF set.

Samples of $t\bar{t}$ produced in association with a Higgs boson ($t\bar{t}H$ in the following) are generated with the PYTHIA 6.425 [?] LO generator and the MRST LO** PDF set [?],

assuming a Higgs boson mass of 125 GeV and considering the $H \rightarrow b\bar{b}$, $c\bar{c}$, gg , and W^+W^- decay modes.

Parton shower and fragmentation are modelled with HERWIG v6.520 [?] in the case of MC@NLO, with PYTHIA 6.421 in the case of ACERMC, and with PYTHIA 6.425 in the case of MADGRAPH. All these samples are generated assuming a top quark mass of 172.5 GeV. The single top quark samples are normalised to the approximate NNLO theoretical cross sections [?, ?] using the MSTW2008 NNLO PDF set, while the $t\bar{t}V$ samples are normalised to the NLO cross section predictions [?, ?]. The $t\bar{t}H$ sample is normalised using the NLO theoretical cross section and branching ratio predictions [?]. Finally, the diboson backgrounds are modelled using HERWIG with the MRST LO** PDF set, and are normalised to their NLO theoretical cross sections [?].

Signal samples

For vector-like T signals, samples corresponding to a singlet T quark decaying to Wb , Zt and Ht are generated with the PROTONS v2.2 LO generator [?, ?] using the MSTW2008 LO PDF set, and interfaced to PYTHIA for the parton shower and fragmentation.

For each decay channel (Wb , Zt and Ht) the branching ratio has been set to 1/3. Events are reweighted in order to reproduce any desired branching ratio configuration.

The predicted branching ratios in the weak-isospin singlet and doublet scenarios as a function of m_T are given in Table 5.2.

The m_T values considered range from 350 GeV to 850 GeV in steps of 50 GeV, with the Higgs boson mass assumed to be 125 GeV. All Higgs boson decay modes are considered, with branching ratios as predicted by HDECAY [?].

Signal samples are normalized to the approximate NNLO theoretical cross sections [?] using the MSTW2008 NNLO PDF set. The cross section values used are summarized in Table 5.3.

m_T (GeV)	$BR(T \rightarrow Wb)$	Singlet		$BR(T \rightarrow Wb)$	Doublet	
		$BR(T \rightarrow Zt)$	$BR(T \rightarrow Ht)$		$BR(T \rightarrow Zt)$	$BR(T \rightarrow Ht)$
350	0.545	0.116	0.338	0.000	0.255	0.745
400	0.513	0.139	0.348	0.000	0.285	0.715
450	0.502	0.158	0.341	0.000	0.316	0.684
500	0.497	0.173	0.330	0.000	0.343	0.657
550	0.495	0.185	0.321	0.000	0.365	0.635
600	0.494	0.194	0.312	0.000	0.383	0.617
650	0.494	0.202	0.304	0.000	0.399	0.601
700	0.494	0.208	0.298	0.000	0.411	0.589
750	0.494	0.214	0.292	0.000	0.422	0.578
800	0.494	0.218	0.288	0.000	0.431	0.569
850	0.494	0.222	0.284	0.000	0.439	0.561

Table 5.2: Branching ratios for T decay as a function of m_T as computed with PROTONS in the weak-isospin singlet and doublet scenarios.

m_T (GeV)	$\sigma(TT)$ (pb)	Scale uncertainties (pb)	PDF+ α_s uncertainties (pb)	Total uncertainty (pb)
350	5.083	+0.140/-0.285	+ 0.569/-0.488	+0.586/-0.565
400	2.296	+0.066/-0.130	+ 0.269/-0.221	+0.277/-0.257
450	1.113	+0.034/-0.063	+ 0.136/-0.107	+0.140/-0.125
500	0.5702	+0.0185/-0.0327	+ 0.0723/-0.0545	+0.0746/-0.0636
550	0.30545	+0.01040/-0.01769	+ 0.04012/-0.02889	+0.0414/-0.0339
600	0.1696	+0.0060/-0.0099	+ 0.0230/-0.0161	+0.0238/-0.0189
650	0.09707	+0.00359/-0.00571	+ 0.01363/-0.00936	+0.01410/-0.01097
700	0.05694	+0.00218/-0.00338	+ 0.00828/-0.00559	+0.00856/-0.00653
750	0.03411	+0.00135/-0.00204	+ 0.00513/-0.00343	+0.00530/-0.00400
800	0.02080	+0.00085/-0.00126	+ 0.00329/-0.00216	+0.00340/-0.00250
850	0.01287	+0.00054/-0.00079	+ 0.00215/-0.00138	+0.00222/-0.00159

Table 5.3: Theoretical cross section at NNLO for TT production as a function of m_T as computed by HATHOR, and scale and PDF uncertainties.

5.3.2 Multi-jet background

QCD production can pass the event selection in the electron channel as non-prompt electrons or as “fake” electrons, i.e. either electrons from photon conversions or mis-identified jets that left a high amount of energy in the electromagnetic calorimeter. For events in the muon channel the main contributions come from non-prompt leptons from semileptonic b - and c -hadron decays.

The contribution to the background from multi-jet events is estimated via data-driven methods, since simulation is not expected to predict this contribution with the desired level of accuracy. The technique used is called “Matrix Method” (MM in the following) [?].

5.4 Systematical uncertainties treatment

779 **Preliminary search for $T\bar{T}$ pairs**
780 **decaying to $Wb + X$**

781

782 **6.1 Boosted W reconstruction**

783 **6.2 Control regions**

784 **6.3 Event selection**

785 **6.4 Systematics**

787 Preliminary search for $T\bar{T}$ pairs
788 decaying to $Ht + X$

789

790 7.1 Control regions

791 7.2 Event selection

792 7.3 Systematics

Results

794

795

8.1 Combination

796

797 **Conclusions**

798

804 **Search for $T\bar{T} \rightarrow Wb + X$ at $\sqrt{7}$ TeV**

805

Bibliography

- [1] J. Aguilar-Saavedra, *Identifying top partners at LHC*, **JHEP** **0911** (2009) 030, [arXiv:0907.3155 \[hep-ph\]](#).
- [2] S. P. Martin, *Extra vector-like matter and the lightest Higgs scalar boson mass in low-energy supersymmetry*, **Phys.Rev.** **D81** (2010) 035004, [arXiv:0910.2732 \[hep-ph\]](#).
- [3] ATLAS Collaboration, *The ATLAS Experiment at the CERN Large Hadron Collider*, **JINST** **3** (2008) S08003.
- [4] L. Evans, P. Bryant (Eds.), *LHC Machine*, **JINST** **3** (2008) S08001.
- [5] CMS Collaboration, *The CMS experiment at the CERN LHC*, **JINST** **3** (2008) S08004.
- [6] ALICE Collaboration, *The ALICE experiment at the CERN LHC*, **JINST** **3** (2008) S08002.
- [7] LHCb Collaboration, *The LCHb experiment at the CERN LHC*, **JINST** **3** (2008) S08005.
- [8] M. Lamont, *The First Years of LHC Operation for Luminosity Production*, in *Proceedings of 4th International Particle Accelerator Conference (IPAC 2013)* (2013) .
- [9] ATLAS Collaboration.
<https://twiki.cern.ch/twiki/bin/view/AtlasPublic/LuminosityPublicResults>.
- [10] ATLAS Collaboration, *Studies of the performance of the ATLAS detector using cosmic-ray muons*, **Eur. Phys. J.** **C** **71** (2011) 1593.
- [11] ATLAS Collaboration, *Readiness of the ATLAS liquid argon calorimeter for LHC collisions*, **Eur. Phys. J.** **C** **70** (2010) 723–753.
- [12] ATLAS Collaboration, *Readiness of the ATLAS Tile calorimeter for LHC collisions*, **Eur. Phys. J.** **C** **70** (2010) 11931236.

- [13] ATLAS Collaboration, *Expected Performance of the ATLAS Experiment - Detector, Trigger and Physics*, [arXiv:0901.0512 \[hep-ex\]](#).
- [14] T. Cornelissen, M. Elsing, S. Fleischmann, W. Liebig, E. Moyse, and A. Salzburger, *Concepts, Design and Implementation of the ATLAS New Tracking (NEWT)*, Tech. Rep. ATL-SOFT-PUB-2007-007. ATL-COM-SOFT-2007-002, CERN, Geneva, Mar, 2007.
- [15] R. Frhwirth, *Application of Kalman filtering to track and vertex fitting*, *Nuclear Instruments and Methods in Physics Research Section A: Accelerators, Spectrometers, Detectors and Applications*, <http://www.sciencedirect.com/science/article/pii/0168900287908874>.
- [16] ATLAS Collaboration, *Performance of primary vertex reconstruction in proton-proton collisions at $\sqrt{s}=7$ TeV in the ATLAS experiment*, Tech. Rep. ATLAS-CONF-2010-069, CERN, Geneva, Jul, 2010.
- [17] ATLAS Collaboration, *Performance of the ATLAS Inner Detector Track and Vertex Reconstruction in the High Pile-Up LHC Environment*, Tech. Rep. ATLAS-CONF-2012-042, CERN, Geneva, Mar, 2012.
- [18] W. Lampl et al., *Calorimeter clustering algorithms: Description and performance*, ATL-LARG-PUB-2008-002 (2012) . <https://cdsweb.cern.ch/record/1099735>.
- [19] ATLAS Collaboration, *Electron performance measurements with the ATLAS detector using the 2010 LHC proton-proton collision data*, *Eur.Phys.J. C* **72** (2012) 1909, [arXiv:1110.3174 \[hep-ex\]](#).
- [20] E. Abat, J. Abdallah, T. Addy, P. Adragna, M. Aharrouche, et al., *Combined performance studies for electrons at the 2004 ATLAS combined test-beam*, *JINST* **5** (2010) P11006.
- [21] B. Acharya, J. Adelman, S. Adomeit, M. Aoki, B. Alvarez, F. Balli, W. Bell, K. Becker, K. Behr, D. Benjamin, E. Bergeaas Kuutmann, C. Bernard, K. Black, S. Calvet, R. Camacho, Y. Coadou, G. Cortiana, N. Cooper-Smith, T. Cornelissen, M. Cristinziani, V. Dao, U. De Sanctis, C. Doglioni, F. Derue, K. Finelli, K. Grahn, J. Groth-Jensen, S. Head, A. Henrichs, D. Hirschebuehl, V. Kaushik, O. Kind, H. Khandanyan, A. Krasznahorkay, T. Kuhl, E. Le Menedeu, H. Lee, A. Lister, K. Loureiro, L. Miljovic, J. Morris, R. Moles Valls, O. Nackenhorst, D. Pelikan, M. Owen, M. Pinamonti, K. Rao, K. Rosbach, M. Rudolph, G. Salamanna, J. Schwindling, J. Searcy, E. Shabalina, K. Shaw, J. Sjolin, R. Soualah, S. Stamm, D. Ta, T. Theveneaux-Pelzer, E. Thompson, K. Uchida, L. Valery, M. Vreeswijk, C. Wasicki, I. Watson, K. Yau, J. Zhong, H. Zhu, and M. zur Nedden, *Object selection and calibration, background estimations and MC samples for the Winter 2013 Top Quark analyses with 2012 data*, Tech. Rep. ATL-COM-PHYS-2013-088, CERN, Geneva, Jan, 2013.
- [22] M. Cacciari, G. P. Salam, and G. Soyez, *The anti- k_t jet clustering algorithm*, *JHEP* **04** (2008) 063, [arXiv:0802.1189v2 \[hep-ph\]](#).

- [23] M. Cacciari and G. P. Salam, *Dispelling the N^3 myth for the k_t jet-finder*,
Phys. Lett. **B641** (2006) 57, [arXiv:0512210v2 \[hep-ph\]](#).
- [24] M. Cacciari, G. P. Salam, and G. Soyez, *FastJet User Manual*,
Eur. Phys. J. **C72** (2012) 1896, [arXiv:1111.6097 \[hep-ph\]](#).
- [25] C. Cojocaru et al., *Hadronic calibration of the ATLAS liquid argon end-cap calorimeter in the pseudorapidity region $1.6 < |\eta| < 1.8$ in beam tests*,
Nucl. Instr. Meth. A **531** (2004) 481, [arXiv:0407009 \[physics\]](#).
- [26] T. Barillari et al., *Local hadronic calibration*, ATL-LARG-PUB-2009-001 (2009) .
<https://cds.cern.ch/record/1112035>.
- [27] ATLAS Collaboration, *Jet energy measurement with the ATLAS detector in proton-proton collisions at $\sqrt{s} = 7$ TeV*, Eur. Phys. J. C **73** (2013) 2304,
[arXiv:1112.6426 \[hep-ex\]](#).
- [28] ATLAS Collaboration, *Commissioning of the ATLAS high-performance b-tagging algorithms in the 7 TeV collision data*, ATLAS-CONF-2011-102 (2011) .
<https://cds.cern.ch/record/1369219>.
- [29] ATLAS Collaboration, *Performance of Missing Transverse Momentum Reconstruction in Proton-Proton Collisions at 7 TeV with ATLAS*, Eur. Phys. J. C **72** (2012) 1844,
[arXiv:1108.5602 \[hep-ex\]](#).

